Pushing the Physical Limits of IoT Devices with Programmable Metasurfaces

Lili Chen [1,2,*], Wenjun Hu[4], Kyle Jamieson[3], Xiaojiang Chen[2], Dingyi Fang[2] and Jeremy Gummeson[1]

[1]Univ. of Massachusetts Amherst, [2]Northwest Univ. (China), [3]Princeton Univ., [4]Yale Univ.

Abstract

Small, low-cost IoT devices are typically equipped with only a single, low-quality antenna, significantly limiting communication range and link quality. In particular, these antennas are typically linearly polarized and therefore susceptible to polarization mismatch, which can easily cause $10-15$ dBm of link loss on communication to and from such devices. In this work, we highlight this under-appreciated issue and propose the augmentation of IoT deployment environments with programmable, RF-sensitive surfaces made of metamaterials. Our smart meta-surface mitigates polarization mismatch by rotating the polarization of signals that pass through or reflect off the surface. We integrate our metasurface into an IoT network as LLAMA, a Low-power Lattice of Actuated Metasurface Antennas, designed for the pervasively used 2.4 GHz ISM band. We optimize LLAMA's metasurface design for both low transmission loss and low cost, to facilitate deployment at scale. We then build an end-to-end system that actuates the metasurface structure to optimize for link performance in real time. Our experimental prototype-based evaluation demonstrates gains in link power of up to 15 dBm, and wireless capacity improvements of 100 and 180 Kbit/s/Hz in through-surface and surface-reflective scenarios, respectively, attributable to the polarization rotation properties of LLAMA's metasurface.

1 Introduction

Internet of Things (IoT) devices have achieved widespread adoption due to shrinking hardware costs and software management tools that ease installation by the end user. In recent years, a wide range of IoT devices have resulted in diverse systems including mobile devices such as smart watches [24] and health trackers or statically deployed devices including sensors, cameras, voice assistants, and other appliance automation [9, 10]. One key property these devices share is low-cost hardware, in particular low-cost radio hardware, allowing for a minimal consumer price point. Such devices are typically deployed by non-experts who understand neither their home's wireless environment nor the deployment considerations that govern wireless performance. Devices are typically deployed in a configuration that is well-suited for a particular application or use-case, but may not be the ideal placement in terms of communications performance. This combination of cheap hardware and non-ideal network topology results in significant opportunities to improve wireless performance.

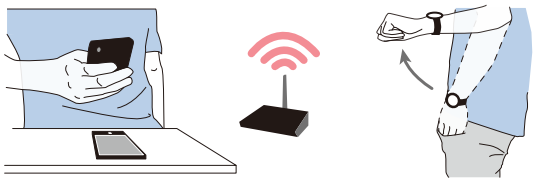

Figure 1: Low-cost IoT devices and wearables suffer from polarization mismatch when their antennas become oriented perpendicularly with respect to their AP's antenna.

One source of performance degradation in such deployments is a significant power loss caused by a *polarization mismatch* [8, 25] between a low-cost dipole antenna on an IoT device and antennas on a Wi-Fi access point (AP)—in higher performance devices (*i.e.*, mobile handsets) this loss is usually mitigated through the use of circularly polarized or dynamically-switched arrangements of linearly polarized antennas in different orientations. Low-cost IoT devices instead use one cheap, linearly polarized dipole antenna structure that results in weak, fragile links between transmitters and receivers. In addition to misaligned statically deployed devices, mobile devices such as wearables, can suffer from dynamic antenna misalignment as a user swings their arm, for example, as Figure 1 illustrates. The effect can be quite significant: microbenchmark experiments show that moving between orthogonal and aligned relative antenna polarization results in ≈ 10 dBm of power variation at the receiver, for both the low power Wi-Fi link between an Arduino [11] and an 802.11g Wi-Fi AP [2] shown in Figure 2 (a), and for the Bluetooth Low

*Work conducted on internship at Univ. of Massachusetts Amherst.

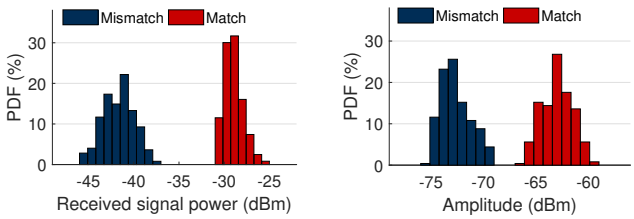

(a) Wi-Fi communication (802.11g) between an access point [2] and a cheap ESP 8266-based Arduino [11].

(b) BLE communication between a wearable sensor (MetaMotionR [23]) and a Raspberry Pi 3 [29].

Figure 2: *Impact of polarization mismatch.* Received signal strength distributions for matching and mismatching antenna orientations between IoT transmitter-receiver pairs. Polarization mismatch significantly reduces link signal strength.

Energy link between a wearable device [23] and a Raspberry Pi 3 [29] shown in Figure 2 (b).

In this work, we investigate how we might be able to change the effective relative orientation of antennas at the communication endpoints, but with no hardware modifications to the endpoints themselves. If we could achieve this objective, we would be able to maintain a low bill of materials cost for IoT wireless communications components, and significantly improve the performance for existing off-the-shelf devices. Our approach to changing effective polarization alignment hinges on instead changing the radio propagation environment itself, with a ***Low-Power Lattice of Actuated Metasurface Antennas*** (*LLAMA*), a tunable smart surface made with inexpensive metamaterials [31,33]. LLAMA is deployed in the radio environment nearby the IoT endpoints, and is able to change the polarization of incident waves as they travel from sender to receiver. As we show in this paper, the LLAMA substrate can be programmed dynamically to effect just the right amount of polarization rotation needed to help the ongoing communication between nearby endpoints.

Designing a metasurface in the 2.4 GHz ISM band requires us to overcome significant challenges. First, since we aim to realize pervasive deployments of these structures, we need to develop materials that are low cost, avoiding high performance but relatively expensive RF materials commonly used in other implementations of metasurfaces. Second, low transmission loss through the metamaterial structure is needed, since the end goal is to provide overall signal improvement. While an inefficient structure could rotate polarization, losses would dominate and the structure would attenuate the incident signal, hampering communication. Overcoming both of these challenges results in a pervasively deployable substrate that can compensate for losses between different endpoint pairs.

Indeed, naively replacing a high performance substrate (*i.e.*, Rogers 5880 [30]) with a low cost substrate (*i.e.*, FR4 [13]) results in higher transmission loss due to FR4's inherent physical properties; this in turn significantly attenuates power at the receiver, reducing link throughput and communication distance. To deal with this problem, we optimize the metasurface structure to ensure the overall system has both low transmission loss, as well as a scalable price point. Specifically, we choose a cheap material (FR4) as the substrate, use a minimum number of substrate layers for the required bandwidth, and minimize the thickness of each layer to significantly reduce the losses associated with FR4.

To enable real-time polarization optimization, a receiver must report received power to a controller which in turn rotates polarization by modifying a pair of bias voltages. Unlike the traditional synchronization methods that require an extra dedicated device [12], LLAMA leverages the fact that the sampling rate of the receiver and the switching speed of power supply are coherent. Hence, we can label the currently received sample by the initial voltage state and current time. We also provide a novel method to estimate the polarization rotation angle induced by the metasurface which can vary with link distance—understanding this mapping is critical in realizing optimal signal improvements.

Contributions. To summarize, LLAMA is the first system that leverages an inexpensive RF substrate to optimize the radio environment in real time, thereby avoiding signal losses caused by polarization mismatch, and thus enables higher quality communication links between IoT devices. In this work, we optimize a metasurface structure based on microwave attenuation theory and achieve comparable polarization tunability to a similar system that uses relatively expensive materials. We validate a proof-of-concept implementation of LLAMA for both communication and sensing with comprehensive experiments. Our results show that LLAMA enables polarization rotation within $3^\circ - 45^\circ$, improves the signal strength by 15 dBm (transmission) and 17 dBm (reflection) with respect to mismatched antenna polarizations. LLAMA also holds great potential to enhance sensing applications, as demonstrated in Section 5.2.2.

2 A Polarizing View of Wireless

Electromagnetic polarization describes the parametric trajectory of the electric and magnetic field vectors of an electromagnetic plane wave as it propagates through space. The polarization of RF wave propagation is a fundamental characteristic of wireless communication, but it has not received as much attention as issues like multipath fading and interference. An antenna constrains outgoing or incoming RF propagation to a particular plane. Therefore, communication is only possible if the signal propagation planes at both the transmitter and the receiver are well aligned.

Polarization loss. One challenge in mobile wireless communication links is the significant power loss due to polarization mismatch. Polarization mismatch is a phenomenon where ad-

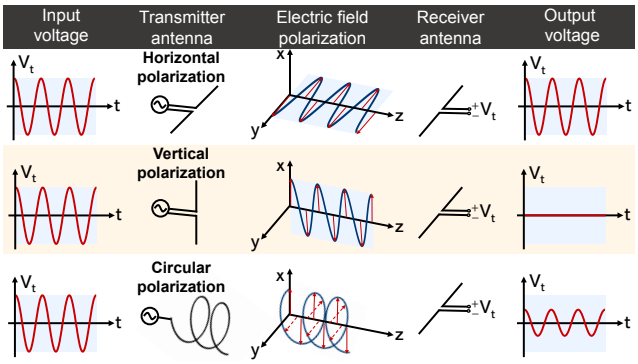

Figure 3: Signal transmission loss under different antenna polarization combinations between transmitter and receiver. When antennas are completely mismatched with orthogonal polarizations, the signal captured by receiver is extremely weak [8].

ditional coupling losses between the transmitter and receiver antennas occur on top of free-space propagation loss if the antennas are not of the same polarization and aligned in space. Three examples of various transmitter antennas and their associated far-field electric fields are depicted in Figure 3. If the signal is being received by a horizontally polarized receiver antenna, it will be polarization matched to the transmitter antenna with horizontal linearly polarized and the power received at the port of the antenna will simply be the input power to the transmitter multiplied by the free space propagation loss. If the transmitter antenna is rotated in space, the received signal will continue to degrade due to polarization mismatch to the point where very little signal is received when the antennas are completely mismatched with orthogonal polarizations. Theoretical 3 dB degradation in coupling due to polarization mismatch will also occur when one of the antennas is circularly polarized while the other is linearly polarized.

As shown in Figure 2, polarization mismatch can be debilitating for IoT devices. Higher performance devices such as mobile phones use switched antennas or circular polarized antennas to mitigate polarization mismatch, but low-cost IoT devices typically have a single low-quality antenna.

Correcting Polarization Mismatch. Intuitively, polarization mismatch can be corrected by rotating the polarization of the signal before it arrives at the receiver. Here we show the mathematical foundation of polarization rotation.

In general, the polarization state of radio waves can be described by a 2×1 Jones vector J. Any polarization state can be represented by two orthogonal components (*i.e.*, in X and Y axes) with different amplitude and phase. The Jones vector is:

$$J = \begin{bmatrix} a \\ be^{j\pi/2} \end{bmatrix}, \tag{1}$$

where a and b represent the amplitude of the X and Y components respectively.

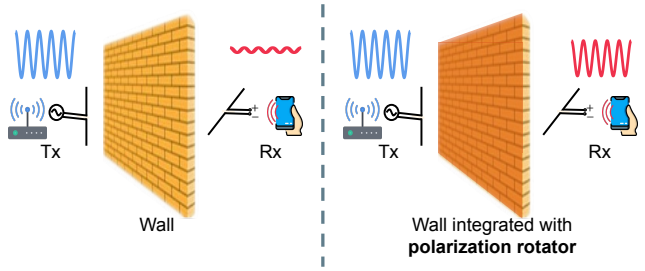

Figure 4: Wireless communication system without/with polarization rotator between mismatched transmitter (Tx) and receiver (Rx).

In systems with multiple layers of polarization manipulation surface between the incident wave and outgoing wave, the outgoing Jones vector is obtained by multiplying the Jones vector of incident wave with the Jones matrix of each surface layer:

$$J_{out} = M_N ... M_2 M_1 J_{in}, \tag{2}$$

where M_N is a 2×2 Jones matrix.

When a manipulation surface is aligned with the x-y coordinate axis, the Jones matrix is represented as:

$$M = e^{j\alpha} \begin{bmatrix} 1 & 0 \\ 0 & e^{j\pi/2} \end{bmatrix}, \tag{3}$$

where α is the common phase delay for the X and Y axes. If the surface is rotated counterclockwise by a degree of θ, the Jones matrix becomes:

$$M_\theta = R(\theta) M R(\theta)^T, \qquad R(\theta) = \begin{bmatrix} \cos\theta & -\sin\theta \\ \sin\theta & \cos\theta \end{bmatrix}, \tag{4}$$

where $R(\theta)$ is the rotation matrix.

To achieve polarization rotation for both x-polarized and y-polarized waves, we construct a polarization rotator consisting of a tunable birefringent structure (BFS) placed between two quarter wave plates (QWP). The QWPs are rotated by $+45^\circ$ and -45° with respect to the BFS, which causes the phase delays for two orthogonal polarizations differ by 90°. The Jones matrices of the two QWPs can be expressed as:

$$Q_{+45^\circ} = e^{j\alpha} R(+45^\circ) \begin{bmatrix} 1 & 0 \\ 0 & e^{j\pi/2} \end{bmatrix} R(+45^\circ), \tag{5}$$

$$Q_{-45^\circ} = e^{j\alpha} R(-45^\circ) \begin{bmatrix} 1 & 0 \\ 0 & e^{j\pi/2} \end{bmatrix} R(-45^\circ). \tag{6}$$

The tunable BFS is a transmissive metasurface that can rotate the polarization of the X and Y axes, independently. The Jones matrix of the BFS is:

$$B = e^{j\beta} \begin{bmatrix} 1 & 0 \\ 0 & e^{j\delta} \end{bmatrix}, \tag{7}$$

where β is the common transmission phase, δ represents the transmission phase difference between X and Y axes, which can be changed by manipulating the biasing voltages of X and Y axes. The entire Jones matrix of the polarization rotator is:

$$P = Q_{+45^\circ} B Q_{-45^\circ} = e^{j(\alpha+(\pi/2)+\beta+(\delta/2))} \begin{bmatrix} \cos(\delta/2) & -\sin(\delta/2) \\ \sin(\delta/2) & \cos(\delta/2) \end{bmatrix}. \quad (8)$$

In summary,the proposed structure can rotate the polarization of a wave by $\delta/2$ rotation degrees, according to the rotation matrix presented in Equation (4).

3 System Design

In this section, we introduce the LLAMA architecture (§ 3.1) and show simulation results obtained from an HFSS simulation environment (§ 3.2). Next, we illustrate our approach towards actuating polarization angle in real-time by manipulating bias voltages for the polarization rotator (in § 3.3). Finally, we describe a technique used to obtain a unique mapping relationship between the polarization rotation degree and received signal power variation to understand the achieved rotation angle at different distances (in § 3.4) .

3.1 System Overview

LLAMA is a low power system that is designed to reduce significant wireless signal loss caused by polarization mismatch between a transmitter and receiver. LLAMA has the ability to improve the communication quality and extend the sensing range in the widely used ISM frequency band.

To achieve this purpose, LLAMA proposes to employ a metasurface-based polarization rotator to deal with the mismatch problem. As shown in Figure 4, the signal from a mismatched transmitter arrives at the receiver with a lower loss when the intermediate wall includes a polarization rotator.

An overview of our system architecture is depicted in Figure 5 and consists of these four elements:

Metasurface. The metasurface used in LLAMA is a polarization rotator implemented using a low-cost FR4 substrate; the polarization rotator is tunable and uses biasing voltages within phase shifters in both the X and Y axes to define a rotation angle. The metasurface is deployed in a structural element (*i.e.*, wall) and influences wireless signals that reflect from or propagate through the metasurface.

Centralized Controller. A centralized controller observes the power measured at a receiver and uses a search algorithm to determine a set of bias voltages that maximize received signal power by finding the optimal rotation angle that achieves a polarization match between the antennas at the endpoints.

Power Supply. The bias voltages used to tune the metasurface are set with a programmable DC power supply. By synchronizing the power supply output with the receiver, we can manipulate the polarization rotator with an optimal rotation angle in real time, with a rotation that maximizes signal power. Two bias voltages are needed for the phase shifters in the X and Y axes; while bias voltages as high as 30 V are needed, the metasurface draws only 15 nA of current. In future implementations, a circuit that generates these bias voltages could be integrated directly on the metasurface.

Endpoints. The endpoint receiver reports its received signal strength to the controller, which then determines how to actuate the metasurface by manipulating the two bias voltages.

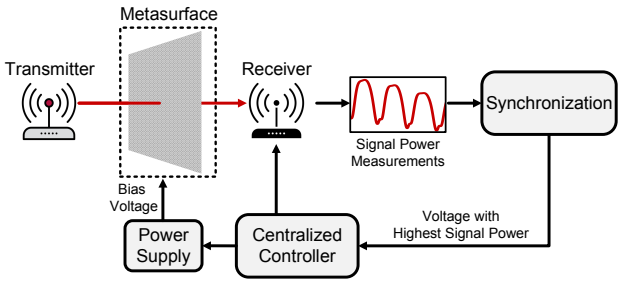

Figure 5: LLAMA system architecture, showing transmitter and receiver endpoints, the LLAMA substrate deployed in the environment, and control signal flow.

3.2 Metasurface Architecture

Tunable metasurfaces are implemented as layered structures that consist of copper patterns printed on controlled dielectric substrates; these layers perform different functions that reflect, bias, or guide EM waves. A transmissive metasurface uses a biasing network sandwiched between or adjacent to wave guide layer(s) to modify the transmissive signal properties in a controlled manner. In contrast, a reflective metasurface uses a reflective metallic plane as one of its layers, where the signal passes through a wave guide and biasing layer, and reflects off the metallic plane in the same relative direction with a different angle of departure. Depending on the bias voltages used LLAMA can operate in either a transmissive or reflective mode, depending on the context of its deployment.

Cost-effective metasurface design. Our simulated polarization rotator was inspired by a 10 GHz design [36] only demonstrated in a highly controlled environment with signal generators and horn antennas; translating this and similar designs into an end-to-end system that can demonstrate control over signal properties (e.g. polarization rotation angle) in realistic environments is the goal of our low-cost metasurface architecture.

In Figure 6 (a) we show the microstrip geometries used in our metasurface design. The surface is comprised of two quarter-wave plates rotated 45° with respect to each other, with an internal pair of biasing layers that controls the polarization direction. We characterize the behavior of this structure using an HFSS simulation environment to analyze critical

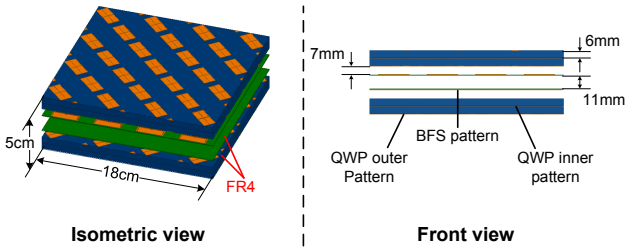

(a) Metasurface structure of LLAMA.

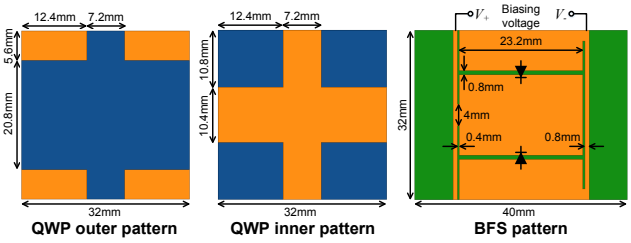

(b) Unit dimension of metasurface unit in LLAMA.

Figure 6: Polarization rotator structure designed for the 2.4 GHz ISM band. The rotator consists of a tunable birefringent structure (green) placed between two quarter wave plates (blue). The tunable birefringent structure acts as a phase shifter that supports different polarization rotations by manipulating its bias voltage of X and Y axis. The metallic patterns (orange) plated on the substrate boards (green and blue) act as admittance components.

parameters in the 2.4 GHz ISM band. In this work, we consider the transmission efficiency (S_{21}) of X and Y axis polarized signals as one of the most important measurement criteria of the overall metasurface design. To better understand the transmission efficiency, here we provide a brief introduction to the scattering matrix S. For a two-port network as shown in Figure 7, the incoming waves (a_1 and b_2) and the outgoing waves (b_1 and a_2) are given by [28]:

$$\begin{cases} a_1 = \frac{V_1+Z_0I_1}{2\sqrt{Z_0}} \\ b_2 = \frac{V_2+Z_0I_2}{2\sqrt{Z_0}} \end{cases}, \quad \begin{cases} b_1 = \frac{V_1-Z_0I_1}{2\sqrt{Z_0}} \\ a_2 = \frac{V_2-Z_0I_2}{2\sqrt{Z_0}} \end{cases}, \tag{9}$$

the scattering matrix S relates the incoming waves to the outgoing waves as [28]:

$$\begin{bmatrix} b_1 \\ b_2 \end{bmatrix} = \begin{bmatrix} S_{11} & S_{12} \\ S_{21} & S_{22} \end{bmatrix} \times \begin{bmatrix} a_1 \\ a_2 \end{bmatrix}, S = \begin{bmatrix} S_{11} & S_{12} \\ S_{21} & S_{22} \end{bmatrix}. \tag{10}$$

S_{11} and S_{22} are reflection coefficients, S_{21} and S_{12} are transmission coefficients. Then the transmission efficiency can be calculated according to following equation [28]:

$$eff = \begin{cases} |S_{21}^{xx}|^2 + |S_{21}^{yx}|^2, & for\ x-polarized\ wave \\ |S_{21}^{xy}|^2 + |S_{21}^{yy}|^2, & for\ y-polarized\ wave \end{cases}, \tag{11}$$

where S_{21}^{yx} means the incoming wave a_1 is in x-polarization mode, and outgoing wave a_2 is in y-polarization mode.

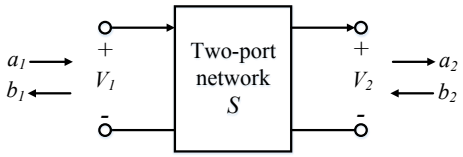

Figure 7: Two-port network [28].

The key challenge in scaling a metasurface structure is determining the correct microstrip feature geometry for inductive and capacitive elements such that the scaled structure will be tuned for the desired frequency band. A key limitation of the design in [36] is its use of an expensive, low-loss dielectric substrate (Rogers 5880). While this material achieves high transmission efficiency (see Figure 8), it is cost prohibitive at scale. In this work, we choose the cheap material substrate FR4 in our design. The key problem is that the FR4 (0.02 dielectric loss tangent) causes much larger signal loss than Rogers 5880 (0.0009 dielectric loss tangent), and thus severely decreases the transmission efficiency, as shown in Figure 9. To deal with this issue, we propose to simplify the structure of tunable phase shifter layers and decrease its thickness, to reduce transmission loss. By comparing Figure 10 and Figure 8, we can see that our optimized structure made of FR4 can achieve comparable transmission efficiency to more complex structures that use low-loss materials.

We use two phase shifting layers, since the transmission bandwidth of a phase shifter changes approximately linearly with the length of the transmission line (*i.e.*, the thickness of phase shifter). Suppose the length of transmission line is λ/m, the bandwidth can be represented as below [28]:

$$\Delta f = f_0(2 - \frac{m}{\pi} arccos[\frac{\Gamma}{\sqrt{1-\Gamma^2}} \frac{2\sqrt{Z_0 Z_L}}{|Z_L - Z_0|}]), \tag{12}$$

where f_0 is the design center frequency of phase shifter, Γ is the maximum tolerable reflection coefficient, Z_0 and Z_L are input impedance and load impedance, respectively. Our two layer design achieves (150 MHz of bandwidth with efficiency > -5 dB), which is wider than the target ISM frequency band that has $<$ than 100 MHz of bandwidth.

Polarization rotation results. Lumped capacitances ranging from 0.84 pF to 2.41 pF were used to approximate a varactor diode (SMV1233) used as part of an LC tank circuit for the X and Y planes; reverse bias voltages from 2 V to 15 V would realize these capacitance values. Here we take x-polarized incident wave as an example to show the polarization rotation results. The transmission efficiencies of the simulated frequencies under various voltage combinations are shown in Figure 11, which are always higher than -8 dB in the $2.4-2.5$ GHz ISM frequency band. The other set of measurements look at how the polarization angle can be controlled by adjusting the lumped tuning capacitance used for the X and Y axis biasing layers. Varying this capacitance from 0.84 pF to 2.41 pF for both the X and Y axes resulted

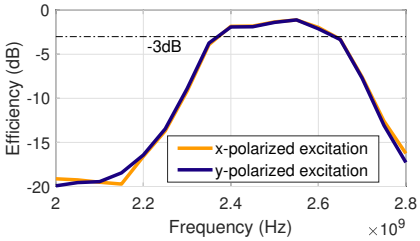

Figure 8: S_{21} efficiency of cascaded polarization rotator layers using Rogers 5880 substrate (loss tangent is 0.0009).

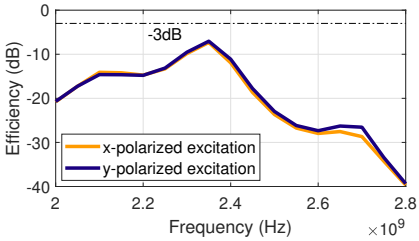

Figure 9: S_{21} efficiency of cascaded polarization rotator layers using FR4 substrate (loss tangent is 0.02).

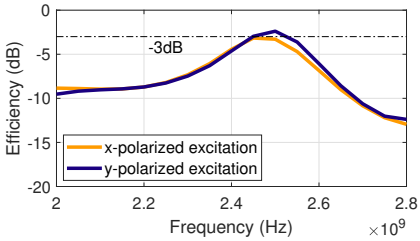

Figure 10: S_{21} efficiency of **optimized** cascaded polarization rotator layers using FR4 substrate (loss tangent is 0.02).

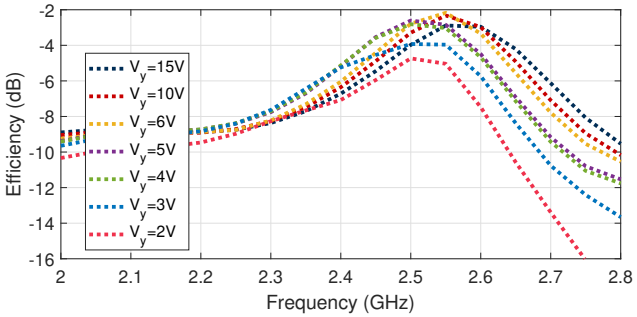

Figure 11: S_{21} efficiencies under different voltage combinations of X and Y axes. The results show polarization can be controlled by changing the biasing voltages of phase shifter.

Table 1: Simulated rotation degrees (θ_r).

θ_r (°)		$V_x(V)$						
		2	3	4	5	6	10	15
$V_y(V)$	2	11.6	26.1	36.8	41.0	44.3	48.3	48.7
	3	6.5	12.4	26.6	32.2	35.2	38.6	39.2
	4	23.0	4.9	10.9	17.3	20.8	25.0	25.6
	5	27.0	9.3	7.4	14.0	18.0	22.6	23.2
	6	41.8	25.0	7.9	2.1	4.2	10.2	10.7
	10	45.8	30.0	13.7	7.9	2.8	5.1	5.6
	15	48.2	33.1	18.2	12.9	7.3	1.9	2.0

in a polarization rotation angle that varied between 1.9° and 48.7° (see Table 1). We have also simulated the polarization rotator structure in the 900 MHz band used for RFID and found comparable performance after additional scaling.

3.3 Metasurface Control

To enable polarization rotation control, we need to change the X and Y axis bias voltages of the integrated phase shifters. For real-time control purposes, we leverage a digitally programmable power supply (Tektronix Series 2230G [3]).

The effective reverse bias voltage of the varactor diodes may need tp be as high as 30 V according to our preliminary tests (due to the fabrication and assemble errors), hence we set 0-30 V as the voltage sweep range of the X and Y axes in our experiments. The power supply is connected to a desktop computer through a USB interface, and is controlled by a Python script that uses the Virtual Instrument Software Architecture (VISA) standard. The voltage switch frequency can be high as 50 Hz. With a voltage step of 1 V, the full scan takes $\sim$ 30 seconds, which prevents real-time applications.

Algorithm 1: Biasing Voltage Sweep

Input: Number of iterations: N; Number of switches for X and Y axes per iteration: T
Initialization: Voltage sweep range of X and Y axes in first iteration ($n=1$): $V_{rx,1}=[v_{x,1}^{min}, v_{x,1}^{max}]$, $V_{ry,1}=[v_{y,1}^{min}, v_{y,1}^{max}]$
for $n=1,...,N$ **do**
  Voltage sweep for X and Y axes in range of $V_{rx,n}$ and $V_{ry,n}$, with step of $V_{s,n}=(v_{x,n}^{max}-v_{x,n}^{min})/T$
end
if *Received signal power at voltage combination* $(v_{x,n,t}, v_{y,n,t})$ *is strongest* **then**
  $n=n+1$, return $V_{rx,n}=[v_{x,n,t}-V_{s,n}, v_{x,n,t}]$ and $V_{ry,n}=[v_{y,n,t}-V_{s,n}, v_{y,n,t}]$
end
Output: Optimal voltage combination: $(v_{x,N,t}, v_{y,N,t})$

To reduce the sweep time, we develop a course-grained to fine-grained sweep mechanism as summarized in Algorithm 1. Specifically, we define N as the number of iterations, T is the number of voltage switches per iteration. $V_{rx,n}$ and $V_{ry,n}$ are the voltage sweep range of X and Y axis in n^{th} iteration, $V_{s,n}$ is the voltage sweep step in n^{th} iteration. So the time cost in n^{th} iteration is $0.02\times N\times T^2$. In this work, we empirically set T and N to 5 and 2, respectively. After N iterations across the X and Y axes, we can determine the optimal voltage combination under which the received signal is strongest.

Synchronization between Rotator and Receiver. For real-time optimal voltage output determination, it is necessary to correlate the current received sample with the bias voltage state. Instead of involving another dedicated device [12], we achieve this purpose by exploiting the fact that the sampling rate of receiver and the voltage switch speed of power supply are constant over time. So we can label the received sample

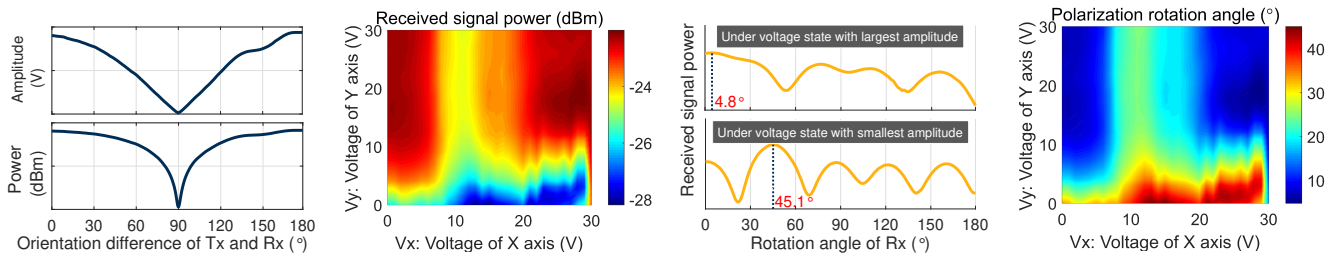

(a) Rx signal power as a function of Tx rotation without metasurface.

(b) Rx signal power with the metasurface in a matched configuration.

(c) Minimum and maximum polarization rotation angle computation.

(d) Polarization rotation angle with metasurface in match setup.

Figure 12: Polarization rotation angle estimation. Figure (a) shows the signal power change pattern over orientation difference between Tx and Rx without metasurface. The polarization rotation degree estimates in Figure (d) are obtained according to the power change slope in (a), power measurements in (b), and minimum and maximum rotation angle estimates in (c). The antenna that needs to be rotated is fixed to a turntable and rotated via remote control.

X_t at time t with voltage state $\{V_{x,t}, V_{y,t}\}$ as below:

$$\{V_{x,t}, V_{y,t}\} = \{V_{x,0} + \frac{VD_x}{T_s} \times (t - t_d), V_{y,0} + \frac{VD_y}{T_s} \times (t - t_d)\}, \tag{13}$$

where $V_{x,0}$ and $V_{y,0}$ represent the voltages of X and Y axes at initial time $t = 0$, VD_x and VD_y are the voltage difference between two adjacent voltage values of X and Y axes, T_s is the time cost of a single voltage switch, t_d is the start time difference between receiver and power supply.

One import thing we want to highlight is that the leaking current of our metasurface is low as 15 nA, which means the metasurface does not need a big battery to power it for a long time, it can work even with one buffer capacitor.

3.4 Polarization Rotation Degree Estimation

Here we present our approach for rotation angle estimation according to the received signal power, no matter the transmitter-receiver distance or the orientation of transmitter. According to our benchmark experimental result plotted in Figure 12 (a), we observed that the received signal power (before the dBm conversion) can be approximated as a linear change with the orientation difference between transmitter and receiver. When we measured the powers after a full sweep of voltages, we can get the maximum power change. To obtain the polarization rotation angle for a unknown transmitter-receiver distance (*i.e.*, the power change slope over orientation difference of transmitter and receiver is unknown), the key is to determine the minimum and maximum polarization rotation angles, which is also the point we are most concerned about in practical applications. We achieved this by following steps.

Step1: Fix the receiver at the same orientation with the transmitter, by rotating the receiver to find a orientation θ_0 where the received power is largest.

Step2: Sweep the voltages to search the voltage combinations V_{min} and V_{max} corresponding to min and max powers, respectively.

Step3: Set the voltage state to the two searched combinations, respectively. At each voltage state, rotate the receiver by 180° to find the new orientation where the power is strongest. The two new orientations of V_{min} and V_{max} can be defined as θ_{max} and θ_{min} as shown in Figure 12 (c). The difference of the receiver's initial orientation and two new orientations $|\theta_0 - \theta min|$ and $|\theta_0 - \theta max|$ correspond to the minimum and maximum polarization rotation angles, respectively.

From the experimental results of the match setup shown in Figure 12 (b-d), we can see that the polarization rotation angle varies between $5° - 45°$ during the voltage sweep.

4 Implementation and Experimental Setup

Metasurface. We fabricated the metasurface with a total surface area of $480 \times 480 \times 5$ mm^3, which includes 180 functional units. The biasing voltages of the X and Y axes of the metasurface are provided by a programmable power supply (TektronixSeries 2230G) through two DC channels, as shown in Figure 13 (a). We connect the power supply to a Linux PC through a USB interface and control the power supply with a Python script that uses the Virtual Instrument Software Architecture (VISA) standard. The output voltage of each channel varies from $0 - 30$ V. LLAMA utilizes 720 varactor diodes, costing $\sim$ 50 cents each. The total cost of LLAMA for all PCB layers is $\sim$ \$540. The total cost of the LLAMA prototype is therefore \$900, with a cost of \$5 per unit. Given economies of scale, we expect the unit cost can be reduced to \$2 when there are more than 3000 units per PCB.

Experimental setup. For controlled experiments, we utilize one USRP N210 software-defined radio with a UBX-40 daughterboard as the ISM signal transceiver, operating at a default center frequency of 2.44 GHz. The transmitter and receiver antennas are separated by a specified distance; We experiment with both directional [6] and omni-directional antennas [1]. We configure and control the USRP using the GNU radio software development toolkit [15] run on a PC. The

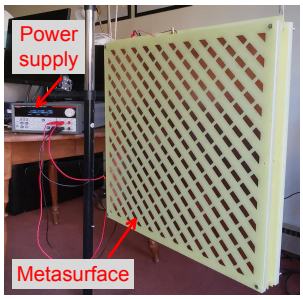

(a) Prototype.

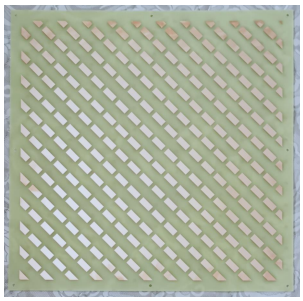

(b) QWP outer layer.

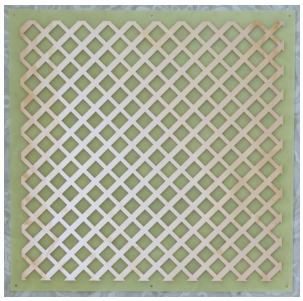

(c) QWP inner layer.

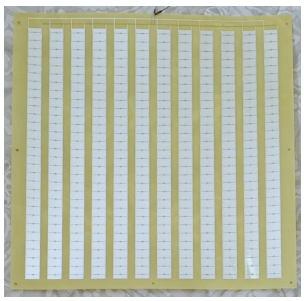

(d) BFS layer.

Figure 13: Prototype of LLAMA. The size of fabricated structure is $480 \times 480 \times 5\ mm^3$ and consists of 180 patterned units.

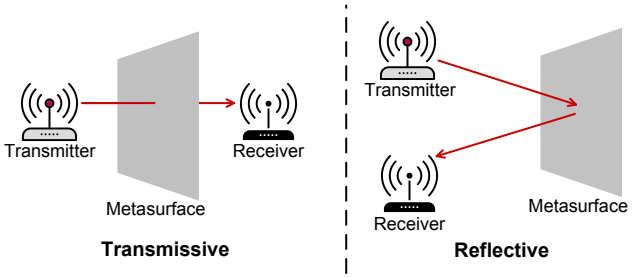

Figure 14: We use two experimental setups in evaluation. The first is a transmissive configuration where endpoints are placed on either side of LLAMA; the second is a reflective configuration where both endpoints are placed on the same side of LLAMA.

transmitter continuously sends a cosine signal over 500 KHz, while the sampling rate of the receiver is 1 MHz. We also evaluate LLAMA using typical low-cost Wi-Fi devices. The communication is between a Wi-Fi AP [2] and a cheap ESP 8266-based Arduino board [11]. The AP can send data at a rate up to 340 Mbps.

We perform both through-surface (*transmissive*) and surface-reflection (*reflective*) experiments. In transmissive experiments, the metasurface is placed between the transmitter and receiver as shown in Figure 14 (left). In reflective experiments, the transmitter and receiver are placed on the same side of the metasurface as shown in 14 (right). In each experiment, the beseline received signal power without the metasurface is measured by averaging 30 seconds of received samples, and the maximum signal power with the metasurface is obtained after a fast sweep of voltages as detailed in section 3.3. To avoid background multipath effects confounding the performance behavior of the LLAMA prototype, we cover the test area with absorbing material, and use directional antennas by default in USRP-based experiments.

5 Evaluation

In this section, we conduct extensive experiments to evaluate the performance of LLAMA. We first answer how metasurface improves the transmissive signal power in mismatch polarization setup. Then we analyze the relationship between signal enhancement induced by metasurface with series of affecting factors including transmitted power, multipath effect, antenna directionality and operating frequency. We also validate LLAMA's ability to enhance reflection signal, and demonstrate the influence of proposed metasurface structure for sensing. In addition, we evaluate LLAMA's performance for practical low-cost IoT communication links.

Performance metrics. We measure signal strength at the receiver as ourr performance metric, since this directly characterizes the benefit of polarization rotation. An increase in the received power usually translates to a throughput improvement. While it is common to measure link throughput directly, the size limit of our current prototype makes it challenging to characterize link throughput in diverse settings.

5.1 Transmissive Operation

5.1.1 Transmissive Signal Enhancement

In this transmissive experiment, we answer three questions: 1) How does the received signal power change according to the bias voltages of the metasurface? 2) What amount of polarization rotation can the metasurface achieve during its biasing voltage sweep? 3) How much can the signal power be increased by using the metasurface?

We conduct experiments under different transmitter-receiver (Tx-Rx) distances (from 24 cm to 60 cm by half wavelength steps of 6 cm). The transmitter and receiver are placed orthogonally such that they are in a mismatched polarization configuration. In each experiment, we measure the received signal power across a full sweep of voltage combinations (both V_x and V_y vary from $0-30$ V).

Figure 15 (a-g) shows how the received signal power changes with different voltage combinations at each Tx-Rx

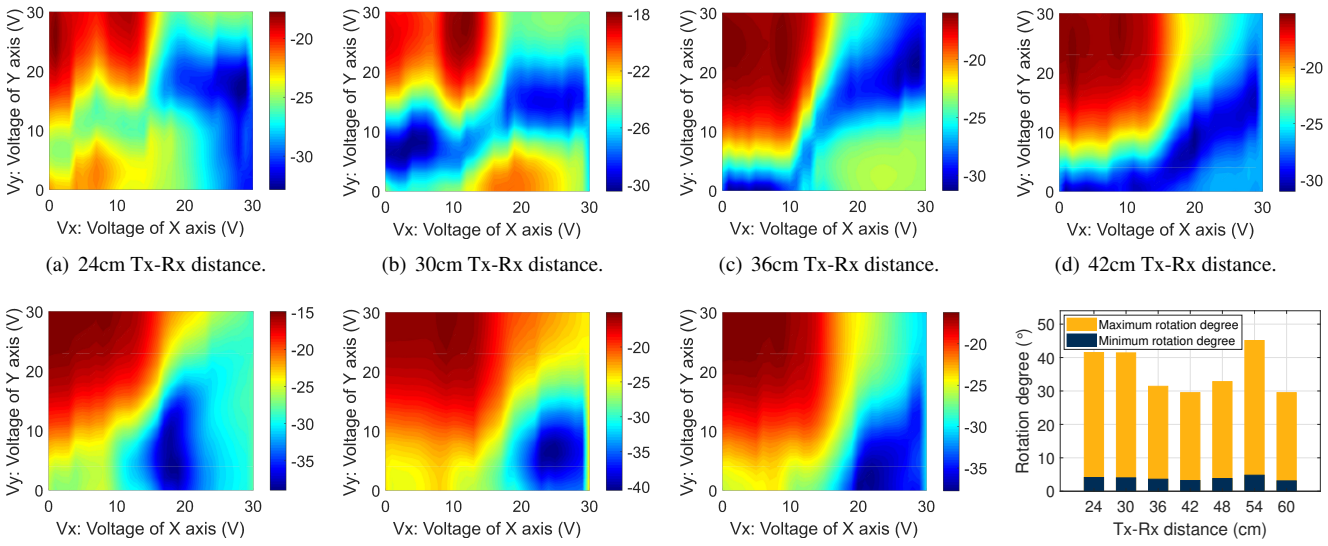

(a) 24cm Tx-Rx distance. (b) 30cm Tx-Rx distance. (c) 36cm Tx-Rx distance. (d) 42cm Tx-Rx distance.

(e) 48cm Tx-Rx distance. (f) 54cm Tx-Rx distance. (g) 60cm Tx-Rx distance. (h) Maximum polarization degree.

Figure 15: Measurements with metasurface under mismatch setup, we do experiments with various Tx-Rx distances. (a-g) show the received signal power heatmap with different voltage combinations. (h) presents the maximum polarization rotation degree caused by metasurface. The testing area is covered with absorber.

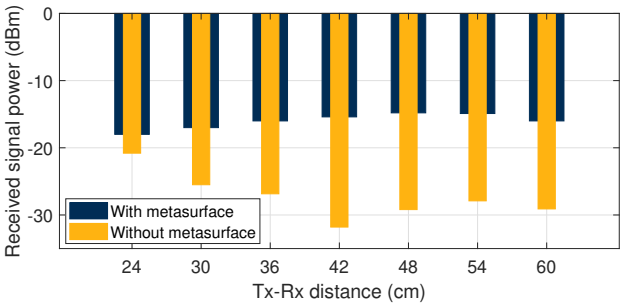

Figure 16: Received signal power with/without metasurface in mismatch polarization.

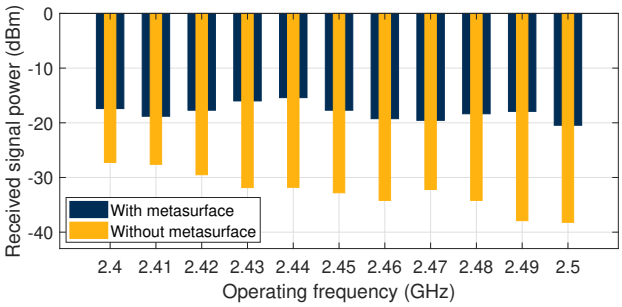

Figure 17: Power improvement VS. operating frequency in mismatch polarization.

distance. The signal power changes significantly with the changes in biasing voltages, we also find the mapping between these voltages as the rotation shifts gradually with respect to Tx-Rx distance. Figure 15 (h) shows the variation of the polarization rotation with respect to distance as measured by the proposed method in section 3.4. We find that the metasurface can rotate the polarization over a range of $3^\circ - 45^\circ$, which allows the metasurface to correct for a significant amount of mismatch.

To understand the signal improvements provided by the metasurface, we also measure the signal power in mismatch configuration with no metasurface present as a baseline. By comparing the results with and without the metasurface as depicted in Figure 16, we can see that the metasurface enhances the transmissive signal power by up to 15 dBm, which extends the potential transmission distance by up to 5.6× according to the Friis transmission equation [14].

5.1.2 Performance Benchmarks

Impact of operating frequency. In order to evaluate LLAMA's performance over the entire ISM frequency band, we conduct experiments that vary the operating frequency from 2.4 GHz to 2.5 GHz by steps of 0.01 GHz. We measure the maximum signal power with and without the metasurface. From the results shown in Figure 17, we can see that LLAMA enables $>$ 10 dBm signal enhancement across the entire ISM frequency band, when compensating for polarization mismatch (orthogonal antenna orientation). This indicates that LLAMA has potential for optimizing IoT communication links with protocols including Wi-Fi, Bluetooth and Zigbee.

Impact of transmit power. In this experiment, we study how transmit power affects the channel capacity enhancement provided by the metasurface. The capacity is calculated according to the SNR measurement and channel bandwidth. We

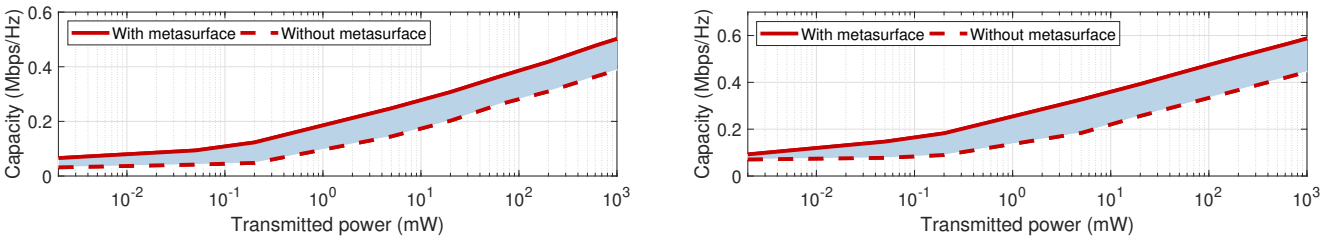

(a) Omni-directional antenna.

(b) Directional antenna.

Figure 18: Impact of transmit power. The experiments are performed in a clean RF environment. We cover the testing area with absorbing material to avoid multipath.

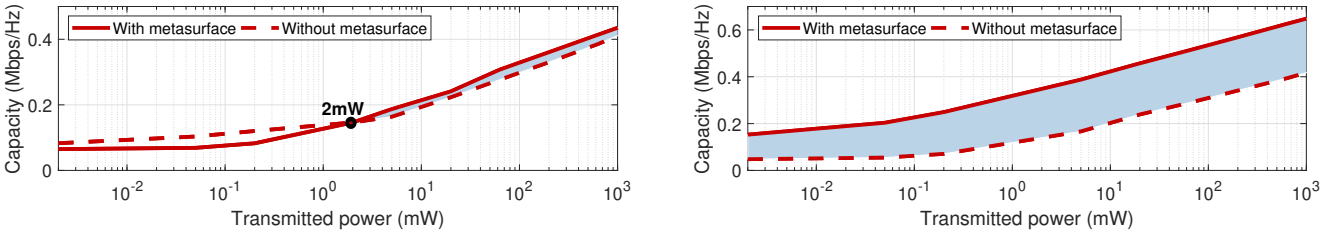

(a) Omni-directional antenna.

(b) Directional antenna.

Figure 19: Experimental results in a rich multipath environment (laboratory). Figure (a) indicates that LLAMA is able to improve signal power as long as the transmitting power is higher than 2 mW even with multipath effect.

perform experiments with both directional [6] and omnidirectional [1] antennas on the transceiver. The transmitting power is changed from 0.002 mW to 1 W. According to the experimental results presented in Figure 18, we observe that the capacity increases slowly with transmitting power for both the directional and omnidirectional antennas; the metasurface can increase the wireless capacity when the transmit power is as low as 0.002 mW.

Impact of multipath. In these experiments we seek to understand the impact of multipath propagation on LLAMA's performance. For this purpose, we perform experiments in an indoor environment (laboratory) without using absorber material. We also measure the channel capacity by using two types of antenna and under various transmitting power. From the results show in Figure 19, we find that for directional antenna, the metasurface can still contribute similar capacity increment as without multipath. This is expected because of the directionality of antenna makes it more robust to multipath. The results from omni-directional atennas are different – when the transmitted power is lower than 2 mW, the metasurface will no longer enhance, and in fact degrade the channel capacity. The reason is the gain of the omni-directional antenna (6 dBi) is lower than that of the directional antenna (10 dBi); when transmitted power is too low, the loss incurred by the metasurface will be greater than the increment of improvement; also when the metasurface is not present, the multipath reflections introduced by the environment cause the received signal to be

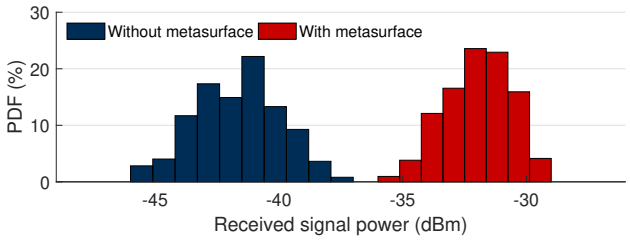

Figure 20: Experimental results of low-cost IoT devices with/without metasurface in polarization mismatch setup.

stronger than with no multipath component.

As is the case with previous environment-based approaches [7, 21], the amount of signal quality change that can be effected by LLAMA depends on the incident power at the metasurface. Since we cannot accurately measure this, Figure 19 (a) reported the transmit power from the endpoints placed at the same location as a proxy for the incident power. This experiment suggests that LLAMA may perform poorly for BLE *transmitters*. Nevertheless, we believe LLAMA could still help Bluetooth *receivers* when the transmitter is a higher-power device, such as a mobile handset.

5.1.3 Experiments with Low-cost IoT Devices

Finally, we evaluate LLAMA's performance with low-cost IoT devices. We perform tests with a common type Wi-Fi

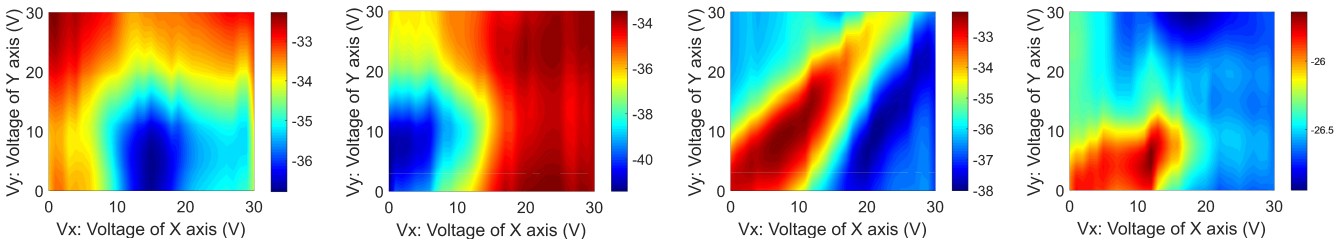

(a) 24cm Tx-Metasurface distance. (b) 30cm Tx-Metasurface distance. (c) 36cm Tx-Metasurface distance. (d) 42cm Tx-Metasurface distance.

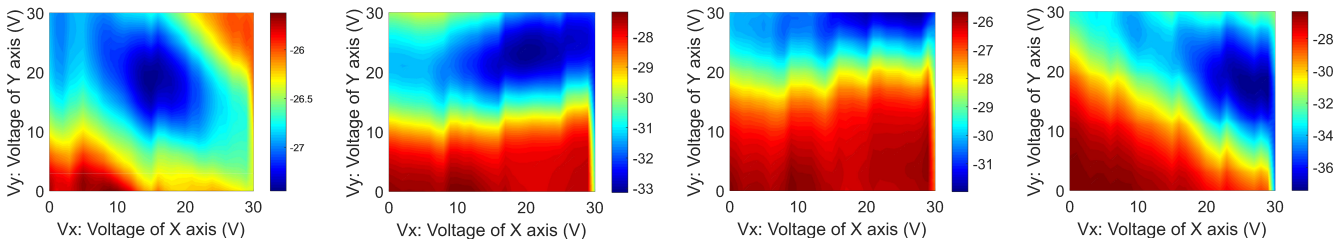

(e) 48cm Tx-Metasurface distance. (f) 54cm Tx-Metasurface distance. (g) 60cm Tx-Metasurface distance. (h) 66cm Tx-Metasurface distance.

Figure 21: Experimental results in reflection scenario. The transmitter and receiver are placed on the same side of the metasurface (See Figure 14). We find that LLAMA also changes the reflective signal power in a polarization mismatch configuration across increasing distance from the metasurface.

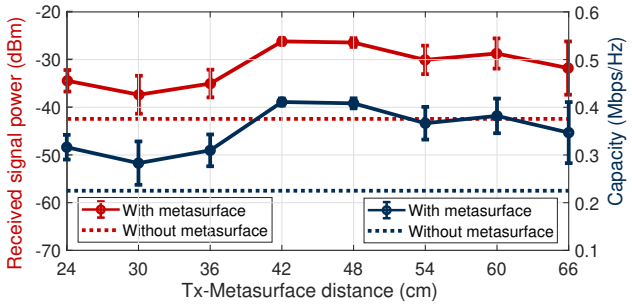

Figure 22: LLAMA provides improvements to channel capacity and power in a reflective configuration.

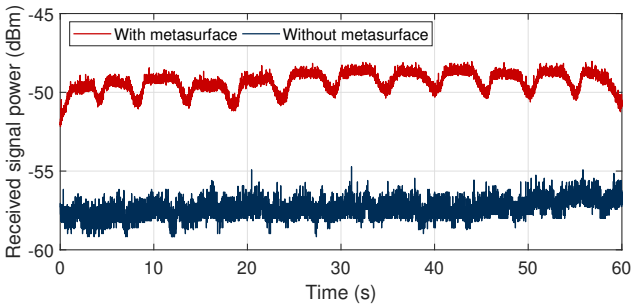

Figure 23: Human respiration sensing results with/without metasurface at low transmitting power 5 mW.

link; communication is between a Wi-Fi router and a cheap Arduino based on an ESP8266 SoC. From the signal power distributions shown in Figure 20, we can see that LLAMA creates around 10 dBm signal power increment in mismatch polarization setup, which looks similar to the matched configuration depicted in Figure 2. This further validates the effectiveness of LLAMA. We believe LLAMA also has great potential to enhance other low-cost IoT communication links such as Zigbee or Bluetooth Low Energy.

5.2 Reflective Operation

5.2.1 Reflective Signal Enhancement

In addition to evaluating transmissive configurations, we also look at LLAMA's affect on reflected signals. We place the transmitter and receiver on the same side of the metasurface, and separate the transmitter and receiver by 70 cm. We perform experiments at different transmitter/metasurface distances by moving the metasurface along the vertical line of the transceiver pair. Figure 22 shows the received signal power changes with the metasurface over a full sweep of voltage combination, as well as the baseline measurements without the metasurface in a mismatched configuration. These results show that LLAMA also improves received signal power and channel capacity in a reflection configuration – the signal power and capacity can be improved with respect to mismatch by as much as 17 dBm and 180 kbps/Hz, respectively. However, the signal power difference over different voltage combinations is much smaller than that in the transmission scenario as shown in Figure 21. We believe this is because the rotation will be cancelled after the signal is reflected.

5.2.2 Employing LLAMA for Sensing

Based on the reflective configuration, we conjecture that LLAMA can be utilized to enhance sensing. To validate this, we consider human respiration detection as a case study to test LLAMA's potential. In this experiment, the metasurface is placed 2 *m* away from the center of the transceiver pair that is separated by 70 *cm*, the human subject is located between the transceiver pair and the metasurface, and on the side between the transmitter and the metasurface. First, we remove the metasurface and reduce the transmitting power to where (5 *mW*) the human subject's respiration can no longer be detected from the received signal. Then we introduce the metasurface at the predetermined location, and measure the received signal strength. The detection results with and without the metasurface are plotted in Figure 23. It is clear that the metasurface can enhance the reflected signal and allow the target's respiration rate to be detectable under a low transmit power configuration. We believe that LLAMA can also be extended to other low SNR sensing applications [16, 38].

6 Related Work

Broadly speaking, our work is related to literature in the following three areas.

Endpoint optimizations. Most efforts for improving communication quality focuses on controlling the endpoints themselves. For instance, Multiple Input, Multiple Output (MIMO) links leverage multiple antennas to exploit spatial diversity at a sub-link level, while Multi-User MIMO exploits spatial diversity at an inter-link level. Massive MIMO introduce many more antennas at an access point than both radio chains and users, so that the AP may search for a set of antennas that forms a well-conditioned MIMO channel to those users [17, 18, 22, 27, 32, 37]. However, these approaches are fundamentally limited for two reasons. On one hand, for a given wireless channel, there are only a limited number of signal degrees of freedom the endpoints can use to increase throughput and mitigate interference. On the other hand, approaches such as phased arrays and distributed antenna systems rely on bulky and/or expensive transmission lines (*i.e.*, coaxial cables, optical fiber, or waveguides) to distribute the signal among antennas.

In contrast, an approach that changes the environment itself offers the possibility of increasing the number of degrees of freedom, which can be achieved by combining the wireless propagation environment with low-cost reflectors [5, 7, 21, 34].

Environment reflectors. Previous work on radio environment optimizations falls into two categories: phase-based and amplitude-based.

Initial attempts of phase based approaches such as leveraging static mirrors [39] or programmable phased-array reflectors [4, 5] are in the ability of generating constructive propagation paths. These methods focus on millimeter Wave links that are within high frequency bands (*i.e.*, 10 GHz). More recent work, such as LAIA, enables the manipulation of the radio environment in a lower frequency Wi-Fi band, by using a large arrays of inexpensive antennas as phase shifting elements [21, 35]. This system aligns phase elements according to a channel decomposition. However, LAIA's channel decomposition algorithm requires highly accurate channel state information, which is not available in current commodity Wi-Fi devices.

Amplitude-based reflector designs, such as RFocus [7], sidestep the difficulty in measuring phase. According to the signal amplitude measurements from the receiver, RFocus configures he signal to either pass through or reflect off the surface element by setting the "on" or "off" state of each element on the surface, so that the transmitted signal is focused at the intended receiver.

Our work differs from prior work, as prior aim is to align multiple paths; LLAMA is a novel attempt to improve low-cost IoT communication links by overcoming the pervasive issue of polarization mismatch.

Metamaterials. Recent work in the applied physics community has developed metamaterials that can directly alter existing signals in the environment itself, including negative refraction index [20], engineering complex beam patterns [26], and changing the polarization of wireless signals [19, 36]. While these metamaterial designs have shown great promise in controlled experiments that quantify performance at 10 GHz and higher, they have not been integrated into an end-to-end system that optimizes signal paths in real time.

In this work, we present an end-to-end system incorporating the structure of a metasurface design for the 2.4 GHz ISM band, and control the structure's polarization rotation to optimize the communication link between a pair of devices.

7 Conclusion

This paper highlights the under-appreciated issue of polarization mismatch for low-cost IoT devices that are physically limited to employing a single low-quality antenna. We present LLAMA, a system designed to mitigate the polarization mismatch without hardware modifications to the IoT devices. LLAMA is capable of manipulating the polarization state of the signal arriving at the receiver with a metasurface structure made with cheap material. It can optimize the communication quality in real time, and enhance the performance of sensing applications. This work marks the first step towards mitigating polarization issues for individual communication links with a LLAMA prototype. Next, we plan to scale up the size of the metasurface for a larger scale deployment and explore more challenging multi-link scenarios. When there are multiple IoT devices in different polarization orientations, tuning the signal polarization can lead to a new form of polarization reuse or access control and improve the network throughput for dense IoT deployments.

Acknowledgements

This material is based upon work supported by the National Science Foundation under Grant Nos. CNS-1763212 and CNS-1763309. Any opinions, findings, and conclusions or recommendations expressed in this material are those of the author(s) and do not necessarily reflect the views of the National Science Foundation.

References

[1] Highfine 2 x 2.4 GHz 6 dBi indoor omni-directional Wi-Fi antenna. Website, 2020.

[2] Netgear n300 wifi cable modem wireless router. Website, 2020.

[3] Series 2230G High Power, 3-Channel Programmable Power Supplies. Website, 2020.

[4] O. Abari, D. Bharadia, A. Duffield, D. Katabi. Cutting the cord in virtual reality. *Proceedings of the 15th ACM Workshop on Hot Topics in Networks*, 162–168, 2016.

[5] ——. Enabling high-quality untethered virtual reality. *NSDI*, 531–544, 2017.

[6] Alfa Network APA-M25 2.4+5GHz Dual Band Indoor Antenna. Website, 2020.

[7] V. Arun, H. Balakrishnan. RFocus: Practical beamforming for small devices. *NSDI*, 1–12, 2020.

[8] S. M. Bowers, A. Safaripour, A. Hajimiri. Dynamic polarization control. *IEEE Journal of Solid-State Circuits*, **50**(5), 1224–1236, 2015.

[9] J. Chan, S. Raju, R. Nandakumar, R. Bly, S. Gollakota. Detecting middle ear fluid using smartphones. *Science translational medicine*, **11**(492), eaav1102, 2019.

[10] J. Chan, T. Rea, S. Gollakota, J. E. Sunshine. Contactless cardiac arrest detection using smart devices. *NPJ digital medicine*, **2**(1), 1–8, 2019.

[11] ESP8266 Wi-Fi Main Board. Website, 2020.

[12] X. Fan, H. Ding, S. Li, M. Sanzari, Y. Zhang, W. Trappe, Z. Han, R. E. Howard. Energy-ball: Wireless power transfer for batteryless internet of things through distributed beamforming. *Proc. of the ACM on IMWUT*, **2**(2), 1–22, 2018.

[13] Standard FR4 TG135 Datasheet. Website, 2020.

[14] Friis transmission equation. Website, 2020.

[15] GNURadio. Website, 2020.

[16] U. Ha, J. Leng, A. Khaddaj, F. Adib. Food and liquid sensing in practical environments using rfids. *NSDI*, 1083–1100, 2020.

[17] E. Hamed, H. Rahul, M. A. Abdelghany, D. Katabi. Real-time distributed MIMO systems. *SIGCOMM*, 412–425, 2016.

[18] E. Hamed, H. Rahul, B. Partov. Chorus: Truly distributed distributed-MIMO. *SIGCOMM*, 461–475, 2018.

[19] J. Hao, Y. Yuan, L. Ran, T. Jiang, J. A. Kong, C. Chan, L. Zhou. Manipulating electromagnetic wave polarizations by anisotropic metamaterials. *Physical review letters*, **99**(6), 063,908, 2007.

[20] I. Kourakis, P. Shukla. Nonlinear propagation of electromagnetic waves in negative-refraction-index composite materials. *Physical Review E*, **72**(1), 016,626, 2005.

[21] Z. Li, Y. Xie, L. Shangguan, R. I. Zelaya, J. Gummeson, W. Hu, K. Jamieson. Towards programming the radio environment with large arrays of inexpensive antennas. *NSDI*, 285–300, 2019.

[22] Y. Ma, Z. Luo, C. Steiger, G. Traverso, F. Adib. Enabling deep-tissue networking for miniature medical devices. *SIGCOMM*, 417–431, 2018.

[23] MetaMotionR. Website, 2018.

[24] R. Nandakumar, V. Iyer, D. Tan, S. Gollakota. Fingerio: Using active sonar for fine-grained finger tracking. *Proceedings of the 2016 CHI Conference on Human Factors in Computing Systems*, 1515–1525, 2016.

[25] M. Okatan, J. Mantese, S. Alpay. Polarization coupling in ferroelectric multilayers. *Physical Review B*, **79**(17), 174,113, 2009.

[26] A. A. Orlov, P. M. Voroshilov, P. A. Belov, Y. S. Kivshar. Engineered optical nonlocality in nanostructured metamaterials. *Physical Review B*, **84**(4), 045,424, 2011.

[27] H. S. Rahul, S. Kumar, D. Katabi. JMB: Scaling wireless capacity with user demands. *SIGCOMM CCR*, **42**(4), 235–246, 2012.

[28] R. S. Rao. *Microwave engineering*. PHI Learning Pvt. Ltd., 2015.

[29] Raspberry Pi 3 Model B+. Website, 2020.

[30] Rogers corporation. Website, 2017.

[31] N.-H. Shen, M. Kafesaki, T. Koschny, L. Zhang, E. N. Economou, C. M. Soukoulis. Broadband blueshift tunable metamaterials and dual-band switches. *Physical Review B*, **79**(16), 161,102, 2009.

[32] C. Shepard, H. Yu, N. Anand, E. Li, T. Marzetta, R. Yang, L. Zhong. Argos: Practical many-antenna base stations. *MobiCom*, 53–64, 2012.

[33] D. Shrekenhamer, W.-C. Chen, W. J. Padilla. Liquid crystal tunable metamaterial absorber. *Physical review letters*, **110**(17), 177,403, 2013.

[34] X. Tan, Z. Sun, J. M. Jornet, D. Pados. Increasing indoor spectrum sharing capacity using smart reflect-array. *ICC*, 1–6. IEEE, 2016.

[35] A. Welkie, L. Shangguan, J. Gummeson, W. Hu, K. Jamieson. Programmable radio environments for smart spaces. *Proceedings of the 16th ACM Workshop on Hot Topics in Networks*, 36–42, 2017.

[36] Z. Wu, Y. Ra'di, A. Grbic. Tunable metasurfaces: A polarization rotator design. *Physical Review X*, **9**(1), 011,036, 2019.

[37] Q. Yang, X. Li, H. Yao, J. Fang, K. Tan, W. Hu, J. Zhang, Y. Zhang. BigStation: Enabling scalable real-time signal processing in large MU-MIMO systems. *SIGCOMM CCR*, **43**(4), 399–410, 2013.

[38] M. Zhao, F. Adib, D. Katabi. Emotion recognition using wireless signals. *MobiCom*, 95–108, 2016.

[39] X. Zhou, Z. Zhang, Y. Zhu, Y. Li, S. Kumar, A. Vahdat, B. Y. Zhao, H. Zheng. Mirror mirror on the ceiling: Flexible wireless links for data centers. *SIGCOMM CCR*, **42**(4), 443–454, 2012.